Virtual Inductance for Stable Operation of Grid-Interactive Voltage Source Inverters

Aswad Adib, *Student Member, IEEE*, and Behrooz Mirafzal, *Senior Member, IEEE*

***Abstract*—In this paper, a feedforward virtual inductance control strategy is developed for the stability of voltage source inverters (VSIs) in weak grids. A weak grid is characterized by a low short-circuit ratio and a low inertia constant, in which VSIs become susceptible to voltage distortions and instability. The proposed feedforward virtual inductance term is integrated into the current control loops of grid-tied VSIs. In this paper, the effectiveness of the virtual inductance control strategy in weak grids is first proved through closed-loop transfer function analysis and then the system's root locus analysis to determine the stability region of the system versus the grid impedance. The developed virtual inductance controller is also verified through laboratory experiments for different weak grid scenarios.**

***Index Terms*—Control of grid-tied inverters, LCL filter, virtual inductance, voltage source inverter (VSI), weak grid.**

I. Introduction

VOLTAGE source inverters (VSIs) act as a necessary interface for grid integration of energy storage systems and renewable energy resources. They are also capable of providing various ancillary services to the utility such as negative sequence compensation, harmonic compensation, power factor correction, and reactive power compensation [1]. However, the operation of VSIs is sensitive to grid abnormalities. The situation is particularly apparent in weak grids and islanded microgrids, as the inverter may become unstable in the presence of large grid impedances [2]–[6].

Weak grids are commonly defined as power grids with a low short-circuit ratio (SCR), i.e., high impedance and a low inertia constant (H) [7]. The varying impedance in weak grids leads to undesirable resonance and stability issues for grid-tied VSIs [2], [3]. Furthermore, the interaction between the control systems and grid distortions can cause instability in weak grids [4], [5]. Specifically, the performance of the phase-locked loop (PLL) starts to degrade with increasing grid impedances and can negatively affect the stability of grid-tied systems. In addition, it has been reported in [6] that the positive feedback gain of anti-islanding methods, which is a mandatory feature for sources like photovoltaic and battery, is restricted for stable operation in weak grids. Therefore, it is apparent that weak grids severely degrade grid-tied inverter stability, and as such, several approaches have been proposed to improve the stability of VSIs in weak grids. Filter and controller parameter design procedures under weak grids were outlined in [2] and [8], striking a trade-off between grid-tied VSI performance and stability. In [4] and [6], stability analysis of grid-tied systems was performed focusing only on the interaction between grid impedance and PLL. The equivalent grid impedance associated with weak grids was canceled through active damping in [3] and [5], with the use of additional circuitry, e.g., full-bridge switching module and sensors. Therefore, an autonomous control strategy to improve the stability of grid-tied VSIs in weak grids without any hardware compensator can be very useful. Delay and impedance phase compensators inserted in the voltage feedforward path of the control schemes were proposed in [9] and [10], respectively, to improve VSI stability in weak grids. However, the compensators affect the steady-state performance of the controllers [10]. To minimize the steady-state error caused by the compensators, current references and power factor angle must be adjusted as described in [10], which complicate the operation and tuning of the controllers under different grid conditions. In this paper, the virtual inductance concept is developed to support stable operation of grid-tied VSIs in weak grids.

Virtual impedance has primarily been employed for active and reactive power sharing between paralleled inverters [11]–[15], where the output impedance of the inverters is expected to be equal. Instead of manipulating circuit parameters to match the impedances, virtual impedance terms were added to match the inverter output impedances and to achieve accurate power sharing. The concept of virtual impedance has been extended to other cases, such as in the stability of dc microgrids with constant power loads [16]–[18], resonance mitigation and power quality improvement through active damping [19], [20], and harmonic compensation in grid-tied inverters and harmonic current sharing in islanded microgrids [21]–[23]. In [24], an impedance-based stability analysis for grid-tied inverters in weak grids was presented through output impedance shaping of the inverter using virtual impedance through a complicated series–parallel structure built on the conventional current control loops of grid-tied VSIs.

In this paper, a feedforward virtual inductance term is introduced in the control scheme for grid-tied VSIs, which stabilizes the grid-tied system without requiring system parameter

Manuscript received May 22, 2018; revised August 18, 2018; accepted September 19, 2018. Date of publication October 12, 2018; date of current version March 29, 2019. This work was supported by the National Science Foundation under Grant ECCS-1351665. *(Corresponding author: Aswad Adib.)*

The authors are with the Electrical and Computer Engineering Department, Kansas State University, Manhattan, KS 66506 USA (e-mail: aswadadib@ksu.edu; mirafzal@ksu.edu).

Color versions of one or more of the figures in this paper are available online at http://ieeexplore.ieee.org.

Digital Object Identifier 10.1109/TIE.2018.2874594

This work is licensed under a Creative Commons Attribution 3.0 License. For more information, see http://creativecommons.org/licenses/by/3.0/

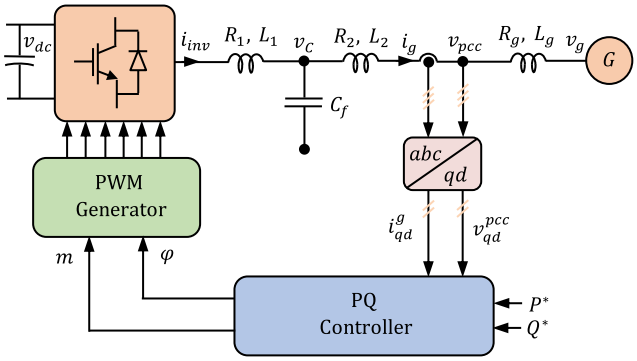

Fig. 1. Schematic diagram of a *PQ*-controlled grid-tied VSI.

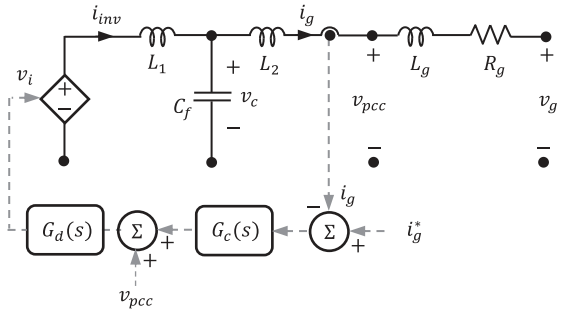

Fig. 2. Simplified schematic diagram of current-controlled VSIs.

redesign while ensuring the system stability. First, it is shown that for a grid-tied VSI employing grid current feedback, the stability can be improved by increasing the inductance of the *LCL* filter. A virtual inductance term is then derived emulating additional inductance in the grid-side *LCL* filter. By introducing the virtual inductance term in the control scheme, the same stabilizing effect of the larger inductance is achieved while avoiding a larger and costlier inverter unit. The proposed strategy can ensure the stability of VSIs in weak grids without deteriorating the steady-state performance of the system, as experimentally demonstrated in this paper. Furthermore, the implementation of the feedforward virtual inductance strategy does not require any additional hardware components, which is an advantage over existing active damping strategies. Therefore, the feedforward virtual inductance control strategy proposed in this paper is well suited for practical applications.

The rest of the paper is organized as follows. In Section II, the impact of filter inductance on VSI stability in weak grids is analytically discussed. In Section III, the virtual inductance term is derived and a state-space model of the closed-loop system including the virtual inductance term is developed. Root locus studies are carried out in Section IV to demonstrate the stabilizing effect of the virtual inductance method in weak grids. The results from Section IV are experimentally verified in Section V. Finally, outcomes are summarized and conclusions are drawn in Section VI.

II. Effect of Filter Inductance on Stability

In this section, the effect of filter inductance on VSI stability in weak grids is discussed, where a more detailed analysis using a full-order VSI model is provided in a later section. The inverter under study is a two-level three-phase VSI equipped with an *LCL* filter, as shown in Fig. 1. For the purposes of this section, a more simplified schematic of the VSI is chosen, as shown in Fig. 2, upon which the analysis is performed.

The inverter is represented by a controlled voltage source in Fig. 2, where a current controller with a transfer function of $G_c(s)$ equipped with voltage feedforward is employed to control the inverter voltage v_i. The delay associated with the control loop is represented by $G_d(s)$. The inverter-side and grid-side inductances of the *LCL* filter are denoted by L_1 and L_2, respectively, whereas the filter capacitance is denoted by C_f. The grid is represented by an equivalent grid inductance L_g and a resistance R_g with a grid voltage of v_g. Also present in Fig. 2 are the point of common coupling (PCC) voltage $v_{\rm pcc}$, capacitor voltage v_c, inverter current $i_{\rm inv}$, grid current i_g, and the desired grid current i_g^*.

Applying KVL on the two loops on both sides of C_f, the voltages can be written as

$$-v_i + L_1 \frac{d}{dt} i_{\rm inv} + v_c = 0, \tag{1}$$

$$-v_c + L_2 \frac{d}{dt} i_g + v_{\rm pcc} = 0. \tag{2}$$

Similarly, $v_{\rm pcc}$ can be written in terms of v_g as

$$v_{\rm pcc} = R_g\, i_g + L_g \frac{d}{dt} i_g + v_g. \tag{3}$$

Furthermore, applying KCL at the capacitor node, the capacitor voltage can be expressed as

$$\frac{d}{dt} v_c = \frac{1}{C_f}\, i_{\rm inv} - \frac{1}{C_f} i_g. \tag{4}$$

Transferring these differential equations into the s-domain and replacing $v_{\rm pcc}$ from (3) in (2) yield

$$s\, I_g = \frac{V_c}{L_2 + L_g} - \frac{V_g}{L_2 + L_g} - \frac{R_g I_g}{L_2 + L_g}. \tag{5}$$

The inverter voltage can also be expressed using the control variables shown in Fig. 2 as follows:

$$V_i = G_d\ (s) \left(V_{\rm pcc} + G_c\,(s) \left(I_g^* - I_g\right)\right). \tag{6}$$

Replacing $V_{\rm pcc}$ from (3) in (6) yields

$$V_i = G_d\ (s) \left(\frac{L_g V_c + L_2 V_g}{L_2 + L_g} + \left(\frac{R_g L_2}{L_2 + L_g} - G_c\,(s) \right) I_g + G_c\,(s)\, I_g^* \right). \tag{7}$$

Replacing V_i from (7) in (1) in the s-domain gives

$$s\, I_{\rm inv} = -\frac{L_2 + L_g\,(1 - G_d)}{L_1\,(L_2 + L_g)} V_c + \left(\frac{G_d R_g L_2}{L_1\,(L_2 + L_g)} - \frac{G_d G_c}{L_1} \right) I_g + \frac{G_d L_2}{L_1\,(L_2 + L_g)} V_g + \frac{G_d G_c}{L_1} I_g^*. \tag{8}$$

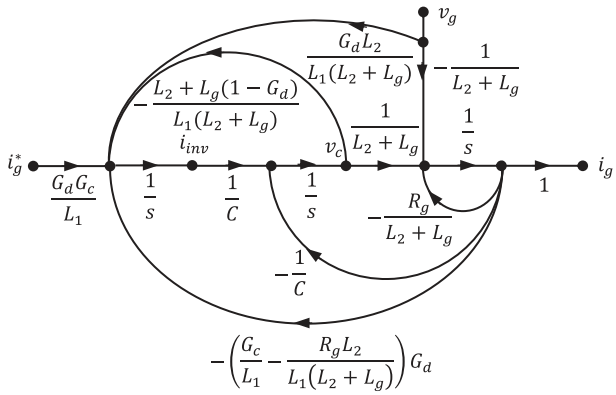

Fig. 3. Signal flow graph of the simplified schematic of the grid-tied VSI shown in Fig. 2.

Now, using (8), (5), and (4) in the s-domain, a lossless signal flow graph of the grid-tied VSI system under study can be drawn, as illustrated in Fig. 3. The output of the current-controlled VSI unit is I_g, while the inputs to the system are I_g^* and V_g. Now, using Mason's rule on the signal flow graph presented in Fig. 3, a transfer function of the system can be derived, i.e., $H(s) = I_g(s)/I_g^*(s) = N(s)/D(s)$, where

$$\begin{cases} N(s) = G_c(s)\, G_d(s) \\ D(s) = s^3 L_1 C_f (L_2 + L_g) + s^2 L_1 C_f R_g \\ \quad + s\left(L_1 + L_2 + L_g\left(1 - G_d(s)\right)\right) \\ \quad + G_c(s)\, G_d(s) + R_g\left(1 - G_d(s)\right) \end{cases}. \tag{9}$$

The denominator can then be expressed in a form suitable for continued-fraction-expansion as

$$\frac{D_1}{D_2} = \frac{s^3 L_1 C_f (L_2 + L_g) + s\left(L_1 + L_2 + L_g\left(1 - G_d(s)\right)\right)}{s^2 L_1 C_f R_g + G_c(s)\, G_d(s) + R_g\left(1 - G_d(s)\right)} \tag{10}$$

where D_1 contains the highest power and the following alternate power terms of the denominator, while D_2 contains the remaining terms. Notice, instead of the continued-fraction-expansion method, one may apply the Routh Hurwitz method. Hence, three criteria must be met for the stability of this system, 1) $(L_2 + L_g) > 0$, 2) $L_1 C_f {R_g}^2 > 0$, and 3) $R_g(L_1 + L_2 G_d(s)) - (L_2 + L_g) G_d(s) G_c(s) > 0$. Since the circuit parameters are all physical parameters and therefore positive, only the third inequality can be applied to extract some information on the system stability. For systems operating in the continuous domain, the control delay can be expressed as $G_d(s) = e^{-sT_d}$ [25], which has a magnitude of $|G_d(s)| = 1$. The third criterion for system stability can then be rewritten as

$$\frac{L_1 + L_2}{L_g + L_2} R_g > \left|G_c(j\omega)\right|. \tag{11}$$

The mathematical expression derived in (11) is an indicator to the effect of various parameters on the stability of the system, whereas a detailed stability analysis through root locus studies is demonstrated in a later section. It can be seen from (11) that for a given control gain, i.e., $|G_c(j\omega)|$, a higher L_g value will result in a lower stability margin. This observation has been already reported by many investigators such as in [3]–[8]. One can also conclude from (11) that an increase in $L_1 + L_2$ can result in a higher stability margin. Apparently, this will be an impractical hardware solution. For an acceptable voltage drop, typically 0.02–0.05 p.u., the maximum boundary of $L_1 + L_2$ can be determined. By limiting the maximum current ripple of the inverter-side inductor in one cycle, the lower and upper boundaries of L_1 can also be obtained [26]. The capacitor C_f and pulsewidth modulation (PWM) frequency can be chosen to avoid the inverter output circuit resonance frequency, i.e.,

$$f_r = \frac{1}{2\pi}\sqrt{\frac{L_1 + (L_2 + L_g)}{L_1 (L_2 + L_g) C_f}}. \tag{12}$$

Moreover, a series resistor R_f with the capacitor C_f can be implemented to further avoid occurrences of resonance at f_r. For the best *LCL* filter performance, $L_2 < L_1$ is selected to satisfy the harmonic restriction standards such as IEEE Std. 1547. The grid-side inductor can also affect the stability of VSIs. Herein, two extreme cases: 1) stiff grids when $L_g \ll L_2$, and 2) weak grids when $L_g \gg L_2$ are assumed. In low-voltage distribution grids, the R/X ratio is typically around 1 [27]. Line impedances could become predominantly resistive, i.e., $R/X > 5$, in islanded microgrids [28]. However, the proposed technique in this paper is valid for inductive and resistive–inductive weak grids with $(R/X) \leq 1$. The inequality expression in (11) can then be written as

$$\begin{cases} \left(1 + \frac{L_1}{L_2}\right) R_g > \left|G_c(j\omega)\right| & \text{for stiff grids} \\ (L_1 + L_2)\left(\frac{R_g}{L_g}\right) > \left|G_c(j\omega)\right| & \text{for weak grids} \end{cases}. \tag{13}$$

As one can see, only under weak grid conditions, an *LCL* filter with a slightly higher value of L_2 can improve the system stability. However, this paper offers a control (software) solution. In the next section, it is demonstrated how a virtual inductance emulating the *LCL* filter inductance can be integrated into the control scheme.

III. State-Space Model of Grid-Tied VSIs

In this section, the virtual inductance term emulating additional inductance in the *LCL* filter is implemented into the *PQ*-control scheme.

A. Virtual Inductance

As described in Section II, increasing the filter inductances could enable stable operation of VSIs in weak grids. In this paper, a virtual inductance term is derived emulating the impact of the filter inductors. Since i_{inv}, the current going through L_1, is not a measured quantity in the *PQ*-control scheme shown in Fig. 1, the virtual inductance term L_{vir} is designed to represent L_2. The impact of L_{vir} will be derived based on the measured grid current i_g. In the following formulas, the resistance R_{vir}, shown in Fig. 4, denotes the equivalent series resistance of the inductors. Performing KVL in the two loops highlighted

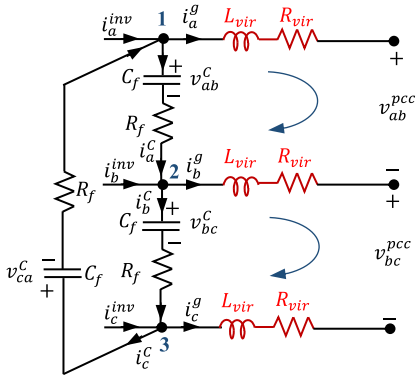

Fig. 4. Schematic diagram of a three-phase VSI focusing on the effect of additional filter inductance on the grid side, which will be added virtually.

in Fig. 4, one can write the following equations:

$$-v_{ab}^C + L_{\text{vir}}\frac{d}{dt}\left(i_a^g - i_b^g\right) + R_{\text{vir}}\left(i_a^g - i_b^g\right) + v_{ab}^{\text{pcc}} - R_f\, i_a^C = 0, \tag{14}$$

$$-v_{bc}^C + L_{\text{vir}}\frac{d}{dt}\left(i_a^g + 2i_b^g\right) + R_{\text{vir}}\left(i_a^g + 2i_b^g\right) + v_{bc}^{\text{pcc}} - R_f\, i_b^C = 0. \tag{15}$$

The current i_c^g in phase-C is replaced in (15) by i_a^g and i_b^g as the system is balanced. By performing KCL in the three numbered nodes shown in Fig. 4, the capacitor currents can be represented with respect to the line currents as

$$i_a^c = \frac{\left(i_a^{\text{inv}} - i_a^g - i_b^{\text{inv}} + i_b^g\right)}{3}, \tag{16}$$

$$i_b^c = \frac{\left(i_a^{\text{inv}} - i_a^g + 2i_b^{\text{inv}} - 2i_b^g\right)}{3}. \tag{17}$$

Replacing the values found in (16) and (17) into (14) and (15), respectively, and solving for the currents going through the virtual inductances, the effect of the virtual inductances on the line currents can be written as

$$i_a^{\text{vir}} = i_a^g = \frac{1}{3R_{\text{vir}}}\left(2v_{ab}^C + v_{bc}^C - 2v_{ab}^{\text{pcc}} - v_{bc}^{\text{pcc}} + R_f i_a^{\text{inv}} - R_f i_a^g - 3L_{\text{vir}}\frac{d}{dt}i_a^g\right), \tag{18}$$

$$i_b^{\text{vir}} = i_b^g = \frac{1}{3R_{\text{vir}}}\left(-v_{ab}^C + v_{bc}^C + v_{ab}^{\text{pcc}} - v_{bc}^{\text{pcc}} + R_f i_b^{\text{inv}} - R_f i_b^g - 3L_{\text{vir}}\frac{d}{dt}i_b^g\right). \tag{19}$$

Since, only the high-frequency current component flows through the capacitor branch, it can be assumed that $i_a^g \approx i_a^{\text{inv}}$, $i_b^g \approx i_b^{\text{inv}}$ by considering only the fundamental current component. In addition, as the equivalent impedances of the filter components are very small, it can be further assumed that $v_{ab}^C \approx v_{ab}^{\text{pcc}}, v_{bc}^C \approx v_{bc}^{\text{pcc}}$. Following these simplifications, (18) and (19) can be rewritten as

$$i_a^{\text{vir}} = -\frac{L_{\text{vir}}}{R_{\text{vir}}}\frac{d}{dt}i_a^g, \tag{20}$$

$$i_b^{\text{vir}} = -\frac{L_{\text{vir}}}{R_{\text{vir}}}\frac{d}{dt}i_b^g. \tag{21}$$

The virtual impedance terms should be converted to the dq frame to be consistent with the controller, which is operating at the dq frame of reference. The Park transformation for a balanced system ($x_a + x_b + x_c = 0$) can be expressed as

$$\begin{bmatrix} x_q \\ x_d \end{bmatrix} = \frac{2}{\sqrt{3}}\begin{bmatrix} -\sin(\theta - 2\pi/3) & \sin(\theta) \\ \cos(\theta - 2\pi/3) & -\cos(\theta) \end{bmatrix}\begin{bmatrix} x_a \\ x_b \end{bmatrix}. \tag{22}$$

Using the dq transformation presented in (22), the virtual impedance terms in (20) and (21) can now be expressed as

$$\begin{bmatrix} i_q^{\text{vir}} \\ i_d^{\text{vir}} \end{bmatrix} = -\frac{L_{\text{vir}}}{R_{\text{vir}}}\frac{d}{dt}\begin{bmatrix} i_q^g \\ i_d^g \end{bmatrix} - \frac{L_{\text{vir}}}{R_{\text{vir}}}\begin{bmatrix} 0 & \omega \\ -\omega & 0 \end{bmatrix}\begin{bmatrix} i_q^g \\ i_d^g \end{bmatrix}. \tag{23}$$

Since the derivative terms have minimal impacts on steady-state conditions, they can be neglected for simplification. The virtual inductance terms in the dq frame of reference then comes out to be as follows:

$$i_q^{\text{vir}} = -\frac{\omega L_{\text{vir}}}{R_{\text{vir}}} i_d^g \tag{24}$$

$$i_d^{\text{vir}} = \frac{\omega L_{\text{vir}}}{R_{\text{vir}}} i_q^g. \tag{25}$$

From (24) and (25), it can be seen that the virtual inductance terms can be expressed in terms of the measured grid currents. As a result, the effect of virtual inductance can be implemented without the need for any additional sensors.

B. PQ Controller Model

In the previous subsection, it was demonstrated through (24) and (25) that the virtual inductance terms have an impact on the grid currents. Hence, the virtual inductance terms should be included in the inner current control loops of the *PQ* control scheme. The complete *PQ* control scheme is shown in Fig. 5. Each controller has two cascaded loops consisting of outer power and inner current control loops, which are equipped with new virtual inductance blocks for stable operation of VSIs in weak grids. The control scheme illustrated in Fig. 5 is based on positive-sequence components for balanced grid voltages. Under unbalanced grid voltages, an independent controller can be added to the control scheme using negative-sequence components of the measured signals. The output of the controllers can then be added to generate the reference signals for PWM generation [29], [30]. As shown in Fig. 5, the *PQ* controller contributes four state variables corresponding to the four integrators that are present in the controller. Replacing P and Q in terms of voltages at PCC and grid currents in their dq frame of reference values as $P = (1/2)(v_q^{\text{pcc}} i_q^L + v_d^{\text{pcc}} i_d^L)$, $Q = (1/2)(v_q^{\text{pcc}} i_d^L - v_d^{\text{pcc}} i_q^L)$ and then linearizing them around a steady-state operating point,

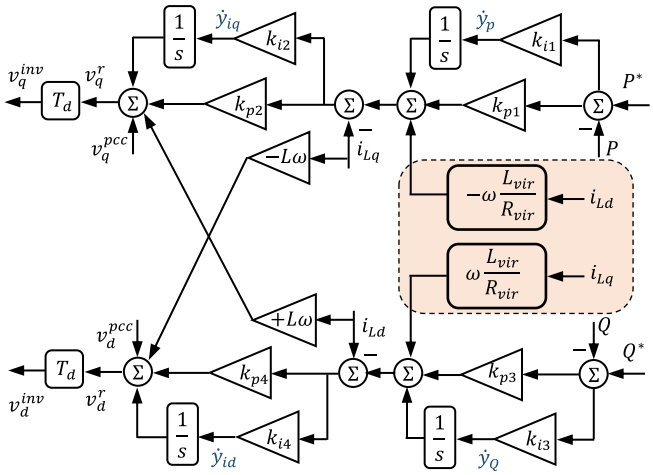

Fig. 5. Control block diagram of a *PQ*-controlled grid-tied VSI with the virtual inductance block highlighted.

the integrator state equations can be written as

$$\dot{y}_P = -\frac{1}{2}k_{i1}V_q^{\rm pcc}i_q^L - \frac{1}{2}k_{i1}I_q^L v_q^{\rm pcc} - \frac{1}{2}k_{i1}I_d^L v_d^{\rm pcc} + k_{i1}P^*, \tag{26}$$

$$\dot{y}_Q = -\frac{1}{2}k_{i3}V_q^{\rm pcc}i_d^L - \frac{1}{2}k_{i3}I_d^L v_q^{\rm pcc} + \frac{1}{2}k_{i3}I_q^L v_d^{\rm pcc} + k_{i3}Q^*, \tag{27}$$

$$\dot{y}_{iq} = k_{i2}\, y_P - k_{i2}\left(\frac{1}{2}k_{p1}V_q^{\rm pcc} + 1\right)i_q^L - k_{i2}\omega\frac{L_{\rm vir}}{R_{\rm vir}}i_d^L + k_{i2}k_{p1}P^* - \frac{1}{2}k_{i2}k_{p1}I_q^L v_q^{\rm pcc} - \frac{1}{2}k_{i2}k_{p1}I_d^L v_d^{\rm pcc}, \tag{28}$$

$$\dot{y}_{id} = k_{i4}\, y_Q + k_{i4}\omega\frac{L_{\rm vir}}{R_{\rm vir}}i_q^L - k_{i4}\left(\frac{1}{2}k_{p3}V_q^{\rm pcc} + 1\right)i_d^L + k_{i4}k_{p3}Q^* - \frac{1}{2}k_{i4}k_{p3}I_d^L v_q^{\rm pcc} + \frac{1}{2}k_{i4}k_{p3}I_q^L v_d^{\rm pcc}. \tag{29}$$

Notice that two input variables P^* and Q^* are also introduced to the model associated with the controller, which represent the desired active and reactive power, respectively.

Furthermore, the delay associated with the controllers can have significant impacts on the stability of the grid-tied system [25]. As shown in Fig. 5, a delay term can be added for continuous time controllers as

$$\dot{v}_q^{\rm inv} = \frac{1}{T_d}\left(v_q^r - v_q^{\rm inv}\right), \tag{30}$$

$$\dot{v}_d^{\rm inv} = \frac{1}{T_d}\left(v_d^r - v_d^{\rm inv}\right). \tag{31}$$

Hence, two new state equations are added to the controller model in (30) and (31), where according to the control scheme shown in Fig. 5

$$v_q^r = v_q^{\rm pcc} + k_{p2}\left(y_P + k_{p1}\left(P^* - P\right) - i_q^L - \frac{\omega L_{\rm vir}}{R_{\rm vir}}i_d^L\right) + \omega L i_d^L + y_{iq}, \tag{32}$$

$$v_d^r = v_d^{\rm pcc} + k_{p4}\left(y_Q + k_{p3}\left(Q^* - Q\right) - i_d^L + \frac{\omega L_{\rm vir}}{R_{\rm vir}}i_q^L\right) - \omega L i_q^L + y_{id}. \tag{33}$$

The state equations with respect to the controller have now been derived. While the developed controller can be connected to any open-loop model for a VSI, a small-signal open-loop circuit model of the VSI is given in the Appendix. The circuit model is averaged over the switching cycle where the typical PWM frequency for grid-tied VSIs is 4–10 kHz. Notice that dominant eigenvalues have frequencies below 750 Hz (∼5000 rad/s) [8], [9], [31]; therefore, the averaging effect on the analysis of the system stability is insignificant. While small signal (linearized) models are commonly employed for stability analysis of VSIs, nonlinear techniques, e.g., Lyapunov stability criterion, can also be applied for the stability analysis; however, selection of a suitable Lyapunov function could significantly complicate the analysis [31], [32]. Therefore, any analysis carried out from a simplified model should be experimentally confirmed in the laboratory.

To integrate the controller model including the virtual inductance block into the circuit model, the control inputs of the open-loop circuit model m and φ have to be replaced with the controller outputs $v_q^{\rm inv}$ and $v_d^{\rm inv}$. By definition of the inverter voltage

$$v_q^{\rm inv} = m v_{\rm dc}\cos(\varphi), \tag{34}$$

$$v_d^{\rm inv} = -m v_{\rm dc}\sin(\psi). \tag{35}$$

Linearizing (34) and (35), m and φ can be written in terms of $v_q^{\rm inv}$ and $v_d^{\rm inv}$ as

$$\begin{bmatrix} m \\ \varphi \end{bmatrix} = \begin{bmatrix} V_{\rm dc}\cos(\Phi) & -MV_{\rm dc}\sin(\Phi) \\ -V_{\rm dc}\sin(\Phi) & -MV_{\rm dc}\cos(\Phi) \end{bmatrix}^{-1} \begin{bmatrix} v_q^{\rm inv} \\ v_d^{\rm inv} \end{bmatrix}. \tag{36}$$

Hence, m and φ can now be replaced in the model by controller state variables. Finally, to include grid characteristics into the model, $v_{\rm pcc}$ is expressed in terms of the grid voltage v_g in the dq frame as

$$\begin{bmatrix} v_q^{\rm pcc} \\ v_d^{\rm pcc} \end{bmatrix} = \begin{bmatrix} R_g & \omega L_g \\ -\omega L_g & R_g \end{bmatrix}\begin{bmatrix} i_q^L \\ i_d^L \end{bmatrix} + L_g\frac{d}{dt}\begin{bmatrix} i_q^L \\ i_d^L \end{bmatrix} + \begin{bmatrix} v_q^g \\ v_d^g \end{bmatrix}. \tag{37}$$

By replacing $v_{\rm pcc}$ by v_g, the completed model of the grid-tied VSI can be derived, which is used for the stability analysis of the system in the next section.

IV. Stability Analysis

In this section, the stability analysis of the grid-tied VSI is performed through root locus studies of the system eigenvalues using the model developed in the previous section. The rated

TABLE I
SYSTEM PARAMETERS

Parameter	Value	Parameter	Value
f	60 Hz	L_1	1 mH
k_{p1}, k_{p3}	0.005	R_1	0.15 Ω
k_{p2}, k_{p4}	0.5	L_2	0.5 mH
k_{i1}, k_{i3}	0.002	R_2	0.1 Ω
k_{i2}, k_{i4}	0.2	C_f	30 μF (Δ)
T_d	390 μs	R_f	0.01 Ω

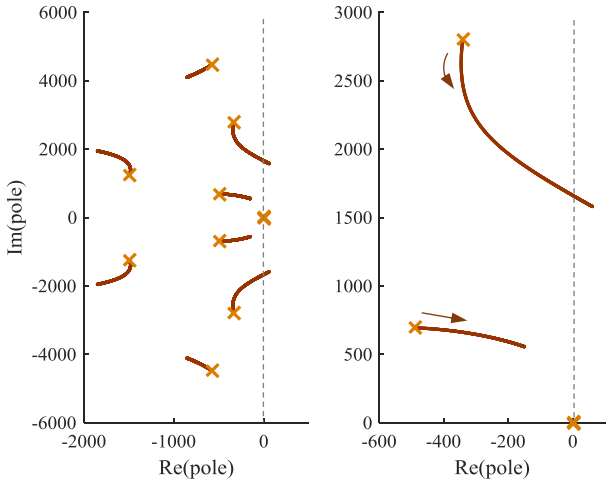

Fig. 6. Root locus of the grid-tied VSI system eigenvalues as L_g is increased from 1.5 mH (cross) to 6 mH without virtual impedance (left), with a zoomed-in plot of the dominant eigenvalues (right).

voltage of the grid-tied system is 240 V with a rated power of 10 kW. The circuit and controller parameters used are presented in Table I. The parameter values listed in Table I are also employed for experimental verification in the next section. Notice that the *LCL* filter parameters are chosen to place the system close to the stability border, and small values for the integrator gains were chosen to avoid overshoots, which could potentially harm the hardware components.

To study the stability of the grid-tied system under weak grids, the root locus of eigenvalues is plotted in Fig. 6 as L_g is gradually changed from 1.5 mH (SCR $=$ 10.2) to 6 mH (SCR $=$ 2.6). The value of R_g is chosen to be 0.2 Ω. For this scenario, the virtual inductance term is not considered and is set to zero. It can be seen in Fig. 6 that as the grid inductance is increased and the grid becomes weaker, the dominant eigenvalues move toward the unstable region and eventually reach the right half-plane, making the system unstable. A zoomed-in version of the dominant eigenvalues is presented in Fig. 6 (right).

Additional inductance in the grid-side *LCL* filter can make the system stable under weak grids. This scenario is illustrated in Fig. 7, where the grid inductance is increased up to 6 mH for a range of L_2 values from 0.5 to 2.5 mH. As shown in Fig. 7, for higher values of L_2, the dominant eigenvalues of the system remain in the left half-plane for the same increase in grid inductance. Hence, a higher L_2 improves the stability of the system in weak grids as expected from the analysis presented in

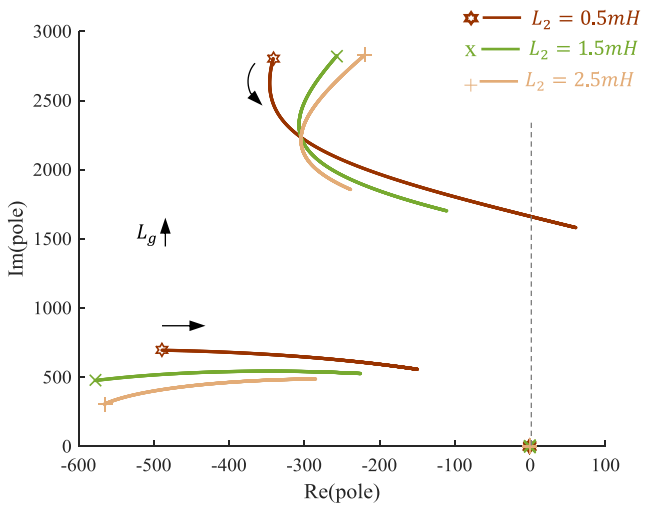

Fig. 7. Root locus of the dominant eigenvalues as L_g is increased from 1.5 to 6 mH for three values of L_2 0.5, 1.5, and 2.5 mH.

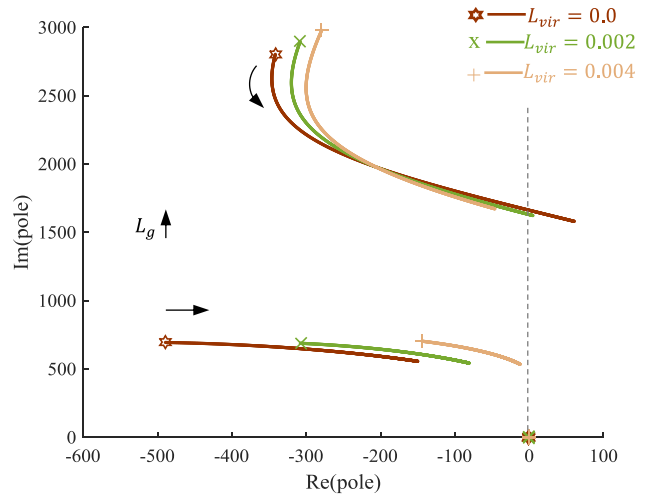

Fig. 8. Root locus of the dominant eigenvalues as L_g is increased from 1.5 to 6 mH for three values of $L_{\rm vir}$ 0, 0.002, and 0.004.

Section II. It can also be seen in Fig. 7 that for smaller values of L_g, the higher L_2 values have a negative impact on stability. Hence, the stabilizing behavior of L_2 is only appropriate in weak grids. However, a higher L_2 will result in a larger and more expensive inverter unit. Therefore, the effect of introducing additional filter inductance will be emulated by the addition of a virtual inductance instead.

In Fig. 8, the root locus of eigenvalues focusing only on the dominant poles is plotted as L_g is increased up to 6 mH for three different values of the virtual inductance $L_{\rm vir}$ ranging from 0 to 0.004. The term $R_{\rm vir}$ is set as $R_{\rm vir} = 1$, as it just acts as an inverse gain for the $L_{\rm vir}$ term as shown in (24) and (25). It can be seen in Fig. 8 that for the larger values of $L_{\rm vir}$, the eigenvalues of the grid-tied system always remain in the stable region similar to the case of L_2. Hence, a grid-tied VSI in weak grids can be operated under stable conditions by introducing a virtual inductance term in its control structure. It should be noted that as the dominant pole of the system remains further

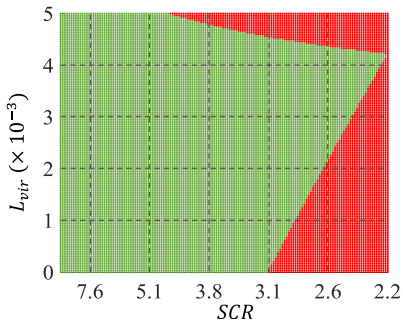

Fig. 9. Stability regions of the grid-tied VSI under weak grids with virtual inductance implemented.

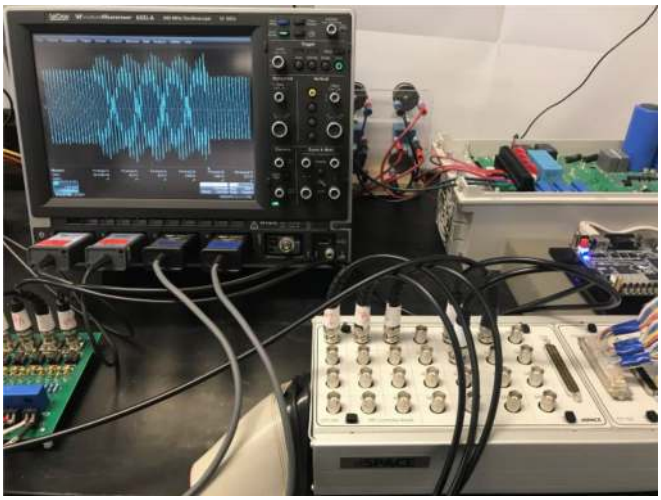

Fig. 10. Experimental setup when the scope display shows the case study demonstrated in Fig. 12.

into the left half-plane as $L_{\rm vir}$ is increased, another pole is seen to be approaching the right half-plane, as illustrated in Fig. 8. Therefore, from a stability perspective, $L_{\rm vir}$ cannot be increased without bounds and there is a range of $L_{\rm vir}$ values for which the system can be kept stable under weak grids. This property of $L_{\rm vir}$ is further demonstrated in Fig. 9 where the stable region is denoted by green and the unstable region is shown by red as $L_{\rm vir}$ is increased, while SCR is decreased, i.e., L_g is increased. It can be seen in Fig. 9 that a virtual inductance term can be designed to keep the system stable under various weak grid conditions. However, as the grid starts to become very weak, the range of $L_{\rm vir}$ values for which the system remains stable becomes restricted. For the operating conditions defined in this section, the virtual inductance can ensure stable operation of the grid-tied VSI up to an SCR value of 2.2.

V. Experimental Results

In this section, the efficacy of the virtual inductance method is verified through experiments carried out on a three-phase grid-tied inverter setup. The experimental setup is shown in Fig. 10. The three-phase inverter used is the power board of an Allen Bradley Powerflex 755. The voltage and current signals were obtained through a measurement board designed in the laboratory and fed to a dSpace CP1103 control board where the *PQ* controller along with the virtual inductance block was built. The PWM references generated through the controller were then fed to an Altera Cyclone III FPGA, which generates the gate signals for the inverter switching module. The system parameters used in these experiments are presented in Table I. For all the experiments carried out in this section, the active power was set to 550 W at unity power factor. The PWM frequency was 5 kHz in these experiments. The current and voltage data were collected using a Lecroy Waverunner 64 Xi-A oscilloscope with CP030 current probes and ADP300 differential voltage probes at a sampling frequency of 100 kHz. The waveforms were then plotted in MATLAB and are presented in this section.

In the first scenario, the system was initially operated under a stiff grid condition, as shown in Fig. 11. The system is stable up to around 2.35 s, when a 5 mH (SCR = 3.1) inductance was inserted between the grid and the PCC that was initially bypassed through a three-phase circuit breaker. As expected, with the introduction of a large grid inductance, the system became unstable. To bring the grid-tied system back to the stable region, a 0.0025 virtual inductance was enabled in the control scheme through Control Desk, a real-time software interface linked with dSpace. As shown in Fig. 11, the virtual inductance term stabilizes the system under a weak grid with 5 mH grid impedance. The test outcome is in agreement with the stability analysis discussed in Section IV, while this scenario can be verified in Fig. 9.

In the second scenario presented in Fig. 12, a grid inductance of 5.5 mH (SCR = 2.8) is inserted into the circuit at 2.2 s, which makes the system unstable. From the stability regions demonstrated through eigenvalue analysis in Fig. 9, it is expected that the grid-tied VSI will return to the stable region if a virtual inductance of 0.0025 is applied to the control scheme. The scenario is verified in Fig. 12, as it can be seen that with the injection of a 0.0025 virtual inductance at 2.5 s the system returns to the stable region of operation following which the controller slowly brings the currents back to the desired operating point.

To validate the efficacy of the virtual inductance scheme under various degrees of weak grid situations, a grid inductance of 6 mH (SCR = 2.6) was inserted into the system at 2.28 s followed by a 0.0025 virtual inductance enabled at 2.5 s, as shown in Fig. 13. Similar to the previous scenarios, the virtual inductance brings the system back to the stable region. This scenario is also in agreement with the stability regions demonstrated in Fig. 9. Notice that if the virtual inductance scheme is kept active from the beginning, as it should be in practical applications, the grid-tied VSI system should stay stable even under weak grid conditions. To demonstrate the effect of the virtual inductance scheme, the virtual inductance has been activated after the system becomes unstable in these case studies.

In the previous scenarios depicted in Figs. 11–13, the efficacy of the virtual inductance scheme in stabilizing VSI operation in weak grids is validated. In the scenario presented in Fig. 14, the output active and reactive power of the VSI are illustrated over a large time period to demonstrate the dynamic and steady-state performances of the system when employing virtual inductance feedforward. In this scenario, a virtual inductance of 0.0003

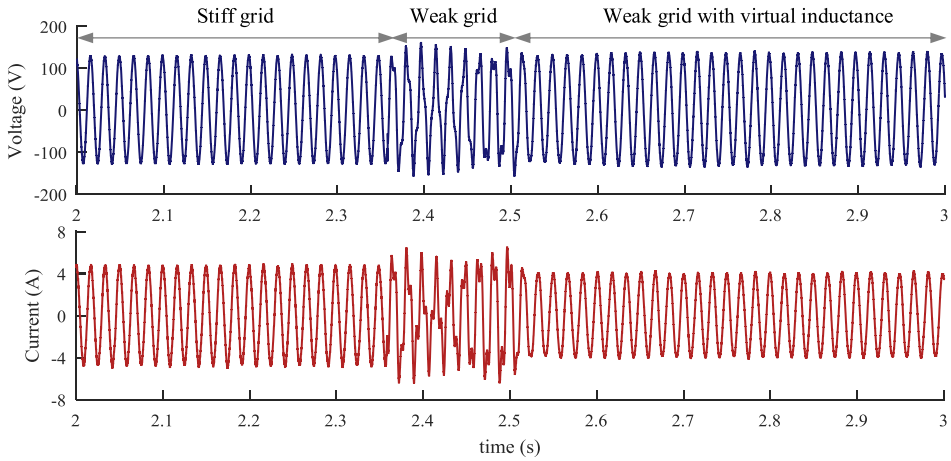

Fig. 11. Voltage at the PCC (top) and grid current (bottom) as $L_g = 5$ mH is inserted at 2.35 s followed by enabling $L_{\rm vir}$ of 0.0025 at 2.5 s.

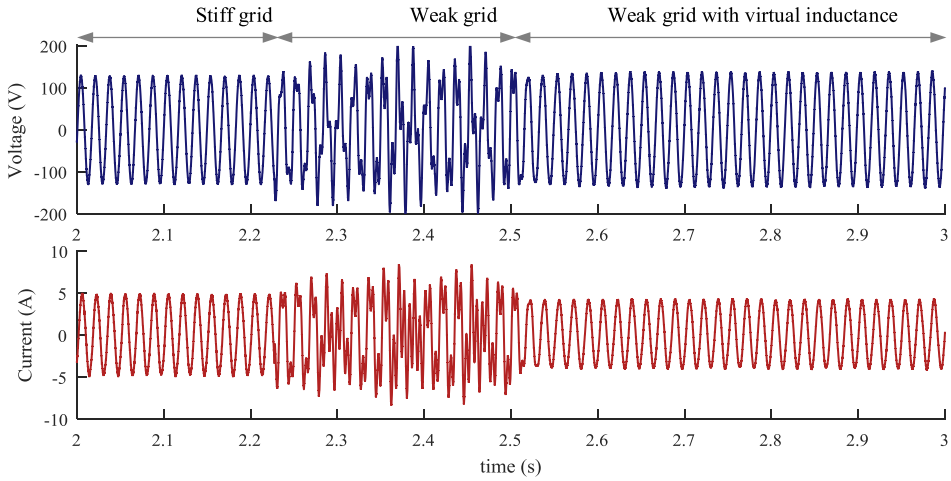

Fig. 12. Voltage at PCC (top) and grid current (bottom) as $L_g = 5.5$ mH is inserted at 2.22 s followed by enabling $L_{\rm vir}$ of 0.0025 at 2.5 s.

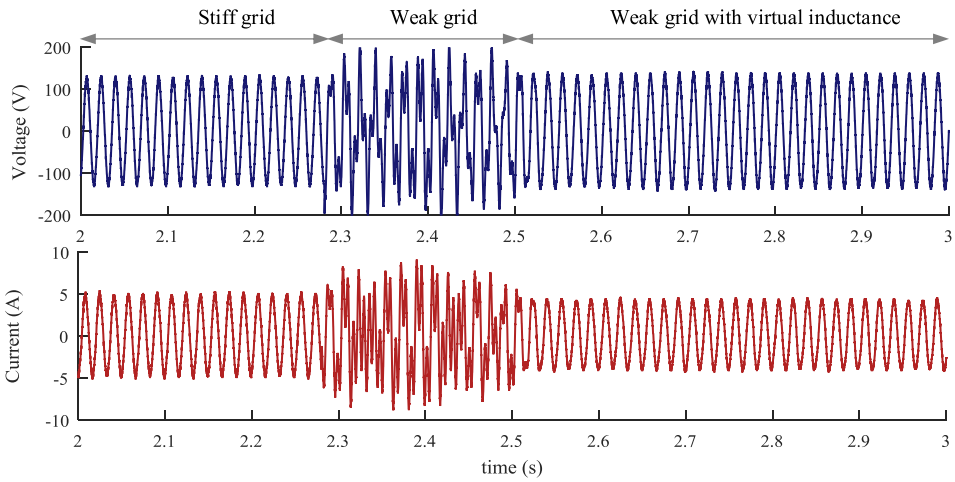

Fig. 13. Voltage at PCC (top) and grid current (bottom) as $L_g = 6$ mH is inserted at 2.28 s followed by enabling $L_{\rm vir}$ of 0.0025 at 2.5 s.

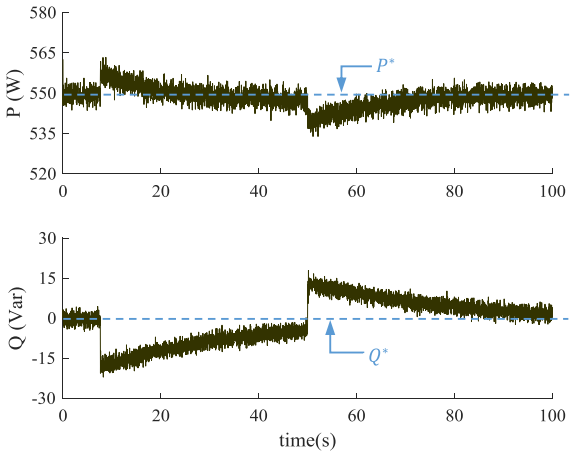

Fig. 14. Active power (top) and reactive power (bottom) supplied by the VSI as a virtual inductance of 0.0003 is introduced at instant 8 s, followed by disabling the virtual inductance term at instant 50 s.

was enabled at instant 8 s into the control scheme of the VSI, which initially deviates the P and Q from their desired values. As shown in Fig. 14, following this deviation, the PQ controllers bring the P and Q back to their reference values, i.e., P^* and Q^*. The virtual inductance term was then disabled at instant 50 s, following which the signals are again restored to their original values. Therefore, the proposed scheme can improve the stability of grid-tied VSIs in weak grids without compromising the steady-state performance.

VI. Conclusion

In this paper, a virtual inductance control strategy was presented to ensure stable operation of grid-tied VSIs in weak grids. A virtual inductance term was derived to emulate additional inductance at the grid-side filter inductance of the *LCL* filter. Increasing the filter inductance could result in stable inverter operation at weak grids as demonstrated analytically in this paper. Instead of physically inserting additional inductance to the *LCL* filter, in this paper, the inductance was added virtually in the control scheme, which allowed avoiding extra cost and hardware modifications while also maintaining the steady-state performance of the system. Furthermore, the virtual inductance term was realized without any additional sensors. A state-space model for a PQ-controlled grid-tied VSI including the virtual inductance feedforward was developed for stability analysis under weak grids. The root locus of eigenvalues indeed showed that the virtual inductance feedforward control scheme can stabilize the grid-tied system in weak grids. The results were verified for three different weak grid scenarios through hardware experiments carried out on a three-phase grid-tied VSI.

Appendix

The open-loop state-space model of the three-phase grid-tied two-level VSI is presented in this appendix only for duplicating the results presented in Section IV. In this model, the states of the circuit model are chosen to be the q and d components of the current out of the inverter $i_{dq}^{\text{inv}} = [\, i_q^{\text{inv}} \;\; i_d^{\text{inv}} \,]^T$, the filter capacitor voltage $v_{dq}^c = [\, v_q^c \;\; v_d^c \,]^T$, and the grid current $i_{dq}^g = [\, i_q^g \;\; i_d^g \,]^T$. The voltages at the PCC $v_{dq}^{\text{pcc}} = [\, v_q^{\text{pcc}} \;\; v_d^{\text{pcc}} \,]^T$ and the inputs to the PWM generator $z = [\, m \;\; \varphi \,]^T$ make up the inputs to the circuit model. Here, m is the modulation index and φ is the phase angle of the inverter voltage with respect to v_{pcc}, which is set as the reference. The state equations can then be written as

$$\frac{d}{dt}\begin{bmatrix} i_{dq}^{\text{inv}} \\ v_{dq}^C \\ i_{dq}^g \end{bmatrix} = \begin{bmatrix} A_{11} & A_{12} & A_{13} \\ A_{21} & A_{22} & A_{23} \\ A_{31} & A_{32} & A_{33} \end{bmatrix} \begin{bmatrix} i_{dq}^{\text{inv}} \\ v_{dq}^C \\ i_{dq}^g \end{bmatrix} + \begin{bmatrix} 0 & B_{12} \\ 0 & 0 \\ B_{31} & 0 \end{bmatrix} \begin{bmatrix} v_{dq}^{\text{pcc}} \\ z \end{bmatrix}. \tag{A1}$$

The A and B block matrices introduced in (A1) are provided as follows:

$$A_{11} = \begin{bmatrix} \frac{-3R_1 - R_f}{3L_1} & -\omega \\ \omega & \frac{-3R_1 - R_f}{3L_1} \end{bmatrix} \quad A_{12} = \begin{bmatrix} \frac{-1}{2L_1} & \frac{\sqrt{3}}{6L_1} \\ \frac{-\sqrt{3}}{6L_1} & \frac{-1}{2L_1} \end{bmatrix}$$

$$A_{13} = \begin{bmatrix} \frac{R_f}{3L_1} & 0 \\ 0 & \frac{R_f}{3L_1} \end{bmatrix} \quad A_{21} = \begin{bmatrix} \frac{1}{2C_f} & \frac{\sqrt{3}}{6C_f} \\ \frac{-\sqrt{3}}{6C_f} & \frac{1}{2C_f} \end{bmatrix}$$

$$A_{22} = \begin{bmatrix} 0 & -\omega \\ \omega & 0 \end{bmatrix} \quad A_{23} = \begin{bmatrix} \frac{-1}{2C_f} & \frac{-\sqrt{3}}{6C_f} \\ \frac{\sqrt{3}}{6C_f} & \frac{-1}{2C_f} \end{bmatrix}$$

$$A_{31} = \begin{bmatrix} \frac{R_f}{3L_2} & 0 \\ 0 & \frac{R_f}{3L_2} \end{bmatrix} \quad A_{32} = \begin{bmatrix} \frac{1}{2L_2} & \frac{-\sqrt{3}}{6L_2} \\ \frac{\sqrt{3}}{6L_2} & \frac{1}{2L_2} \end{bmatrix}$$

$$A_{33} = \begin{bmatrix} \frac{-3R_2 - R_f}{3L_2} & -\omega \\ \omega & \frac{-3R_2 - R_f}{3L_2} \end{bmatrix}$$

$$B_{12} = \begin{bmatrix} \frac{V_{\text{dc}}\cos(\Phi)}{\sqrt{3}L_1} & \frac{-MV_{\text{dc}}\sin(\Phi)}{\sqrt{3}L_1} \\ \frac{-V_{\text{dc}}\sin(\Phi)}{\sqrt{3}L_1} & \frac{-MV_{\text{dc}}\cos(\Phi)}{\sqrt{3}L_1} \end{bmatrix} \quad B_{31} = \begin{bmatrix} \frac{-1}{2L_2} & \frac{\sqrt{3}}{6L_2} \\ \frac{-\sqrt{3}}{6L_2} & \frac{-1}{2L_2} \end{bmatrix}.$$

Acknowledgment

The authors would like to thank R. A. Lukaszewski and Dr. R. M. Tallam of Rockwell Automation, Drives Division for providing an Allen-Bradley Powerflex 755 drive used in the test setup of this work.

References

[1] J. Rocabert, A. Luna, F. Blaabjerg, and P. Rodríguez, "Control of power converters in ac microgrids," *IEEE Trans. Power Electron.*, vol. 27, no. 11, pp. 4734–4749, Nov. 2012.

[2] M. Lu, A. Al-Durra, S. M. Muyeen, S. Leng, P. C. Loh, and F. Blaabjerg, "Benchmarking of stability and robustness against grid impedance variation for LCL-filtered grid-interfacing inverters," *IEEE Trans. Power Electron.*, vol. 33, no. 10, pp. 9033–9046, Oct. 2018.

[3] Y. He, H. S. H. Chung, J. C. T. Lai, X. Zhang, and W. Wu, "Active cancelation of equivalent grid impedance for improving stability and injected power quality of grid-connected inverter under variable grid condition," *IEEE Trans. Power Electron.*, vol. 33, no. 11, pp. 9387–9398, Nov. 2018.
[4] X. Zhang, X. Danni, F. Zhichao, G. Wang, and D. Xu, "An improved feedforward control method considering PLL dynamics to improve weak grid stability of grid-connected inverters," *IEEE Trans. Ind. Appl.*, vol. 54, no. 5, pp. 5143–5151, Sep./Oct. 2018.
[5] S. Zhou *et al.*, "An improved design of current controller for LCL-type grid-connected converter to reduce negative effect of PLL in weak grid," *IEEE Trans. Emerging Sel. Topics Power Electron.*, vol. 6, no. 2, pp. 648–663, Jun. 2018.
[6] B. H. Kim and S. K. Sul, "Stability-oriented design of frequency drift anti-islanding and phase-locked loop under weak grid," *IEEE Trans. Emerging Sel. Topics Power Electron.*, vol. 5, no. 2, pp. 760–774, Jun. 2017.
[7] L. Zhang, L. Harnefors, and H. Nee, "Modeling and control of VSC-HVDC links connected to island systems," *IEEE Trans. Power Syst.*, vol. 26, no. 2, pp. 783–793, May 2011.
[8] A. Adib, B. Mirafzal, X. Wang, and F. Blaabjerg, "On stability of voltage source inverters in weak grids," *IEEE Access*, vol. 6, pp. 4427–4439, 2018.
[9] X. Li, J. Fang, Y. Tang, X. Wu, and Y. Geng, "Capacitor-voltage feedforward with full delay compensation to improve weak grids adaptability of LCL-filtered grid-connected converters for distributed generation systems," *IEEE Trans. Power Electron.*, vol. 33, no. 1, pp. 749–764, Jan. 2018.
[10] X. Chen, Y. Zhang, S. Wang, J. Chen, and C. Gong, "Impedance-phased dynamic control method for grid-connected inverters in a weak grid," *IEEE Trans. Power Electron.*, vol. 32, no. 1, pp. 274–283, Jan. 2017.
[11] J. C. Vasquez, J. M. Guerrero, M. Savaghebi, J. Eloy-Garcia, and R. Teodorescu, "Modeling, analysis, and design of stationary-reference-frame droop-controlled parallel three-phase voltage source inverters," *IEEE Trans. Ind. Electron.*, vol. 60, no. 4, pp. 1271–1280, Apr. 2013.
[12] Y. Zhang, M. Yu, F. Liu, and Y. Kang, "Instantaneous current-sharing control strategy for parallel operation of UPS modules using virtual impedance," *IEEE Trans. Power Electron.*, vol. 28, no. 1, pp. 432–440, Jan. 2013.
[13] J. He, Y. W. Li, J. M. Guerrero, F. Blaabjerg, and J. C. Vasquez, "An islanding microgrid power sharing approach using enhanced virtual impedance control scheme," *IEEE Trans. Power Electron.*, vol. 28, no. 11, pp. 5272–5282, Nov. 2013.
[14] H. Mahmood, D. Michaelson, and J. Jiang, "Accurate reactive power sharing in an islanded microgrid using adaptive virtual impedances," *IEEE Trans. Power Electron.*, vol. 30, no. 3, pp. 1605–1617, Mar. 2015.
[15] C. Li, S. K. Chaudhary, M. Savaghebi, J. C. Vasquez, and J. M. Guerrero, "Power flow analysis for low-voltage ac and dc microgrids considering droop control and virtual impedance," *IEEE Trans. Smart Grid*, vol. 8, no. 6, pp. 2754–2764, Nov. 2017.
[16] X. Lu, K. Sun, J. M. Guerrero, J. C. Vasquez, L. Huang, and J. Wang, "Stability enhancement based on virtual impedance for dc microgrids with constant power loads," *IEEE Trans. Smart Grid*, vol. 6, no. 6, pp. 2770–2783, Nov. 2015.
[17] M. Wu and D. D. C. Lu, "A novel stabilization method of LC input filter with constant power loads without load performance compromise in dc microgrids," *IEEE Trans. Ind. Electron.*, vol. 62, no. 7, pp. 4552–4562, Jul. 2015.
[18] X. Zhang, Q. C. Zhong, and W. L. Ming, "Stabilization of a cascaded dc converter system via adding a virtual adaptive parallel impedance to the input of the load converter," *IEEE Trans. Power Electron.*, vol. 31, no. 3, pp. 1826–1832, Mar. 2016.
[19] X. Wang, F. Blaabjerg, and P. C. Loh, "Grid-current-feedback active damping for LCL resonance in grid-connected voltage-source converters," *IEEE Trans. Power Electron.*, vol. 31, no. 1, pp. 213–223, Jan. 2016.
[20] J. He, Y. W. Li, D. Bosnjak, and B. Harris, "Investigation and active damping of multiple resonances in a parallel-inverter-based microgrid," *IEEE Trans. Power Electron.*, vol. 28, no. 1, pp. 234–246, Jan. 2013.
[21] X. Sun, R. Han, H. Shen, B. Wang, Z. Lu, and Z. Chen, "A double-resistive active power filter system to attenuate harmonic voltages of a radial power distribution feeder," *IEEE Trans. Power Electron.*, vol. 31, no. 9, pp. 6203–6216, Sep. 2016.
[22] P. Sreekumar and V. Khadkikar, "A new virtual harmonic impedance scheme for harmonic power sharing in an islanded microgrid," *IEEE Trans. Power Del.*, vol. 31, no. 3, pp. 936–945, Jun. 2016.
[23] Y. Li *et al.*, "A virtual impedance comprehensive control strategy for the controllably inductive power filtering system," *IEEE Trans. Power Electron.*, vol. 32, no. 2, pp. 920–926, Feb. 2017.
[24] D. Yang, X. Ruan, and H. Wu, "Impedance shaping of the grid-connected inverter with LCL filter to improve its adaptability to the weak grid condition," *IEEE Trans. Power Electron.*, vol. 29, no. 11, pp. 5795–5805, Nov. 2014.
[25] J. Wang, J. D. Yan, L. Jiang, and J. Zou, "Delay-dependent stability of single-loop controlled grid-connected inverters with LCL filters," *IEEE Trans. Power Electron.*, vol. 31, no. 1, pp. 743–757, Jan. 2016.
[26] X. Ruan, X. Wang, D. Pan, D. Yang, W. Li, and C. Bao, *Control Techniques for LCL-Type Grid-Connected Inverters*. New York, NY, USA: Springer, 2018.
[27] A. Moawwad, V. Khadkikar, and J. L. Kirtley, "A new P-Q-V droop control method for an interline photovoltaic (I-PV) power system," *IEEE Trans. Power Del.*, vol. 28, no. 2, pp. 658–668, Apr. 2013.
[28] T. L. Vandoorn, J. D. M. De Kooning, B. Meersman, J. M. Guerrero, and L. Vandevelde, "Automatic power-sharing modification of *P/V* droop controllers in low-voltage resistive microgrids," *IEEE Trans. Power Del.*, vol. 27, no. 4, pp. 2318–2325, Oct. 2012.
[29] F. Blaabjerg, R. Teodorescu, M. Liserre, and A. V. Timbus, "Overview of control and grid synchronization for distributed power generation systems," *IEEE Trans. Ind. Electron.*, vol. 53, no. 5, pp. 1398–1409, Oct. 2006.
[30] A. Adib, J. Lamb, and B. Mirafzal, "Ancillary services via VSIs in microgrids with maximum dc-bus voltage utilization," *IEEE Trans. Ind. Appl.*, to be published, doi: 10.1109/TIA.2018.2865483.
[31] V. Salis, A. Costabeber, S. M. Cox, and P. Zanchetta, "Stability assessment of power-converter-based ac systems by LTP theory: Eigenvalue analysis and harmonic impedance estimation," *IEEE Trans. Emerging Sel. Topics Power Electron.*, vol. 5, no. 4, pp. 1513–1525, Dec. 2017.
[32] K. Acharya, S. K. Mazumder, and I. Basu, "Reaching criterion of a three-phase voltage-source inverter operating with passive and nonlinear loads and its impact on global stability," *IEEE Trans. Ind. Electron.*, vol. 55, no. 4, pp. 1795–1812, Apr. 2008.

Aswad Adib (S'14) was born in Chandpur, Bangladesh, in 1988. He received the B.Sc. degree in electrical and electronic engineering from Bangladesh University of Engineering and Technology, Dhaka, Bangladesh, in 2012. He is currently working toward the Ph.D. degree at Kansas State University, Manhattan, KS, USA.

He worked as a Software Engineer with Samsung R&D Institute Bangladesh, from 2012 to 2014. His research interests include power electronics, dynamic modeling and stability analysis of grid-interactive power converters, and stability of low-inertia microgrids.

Behrooz Mirafzal (S'01–M'05–SM'07) received the Ph.D. degree in electrical engineering from Marquette University, Milwaukee, WI, USA, in 2005.

From 2005 to 2008, he was a Senior Development/Project Engineer with Rockwell Automation/Allen-Bradley, Mequon, WI, where he was involved in research and development related to motor-drive systems. From 2008 to 2011, he was an Assistant Professor with Florida International University, Miami, FL. He is currently an Associate Professor with Kansas State University, Manhattan, KS, USA. He has authored or coauthored more than 80 articles in professional journals and conferences and holds four U.S. patents. His current research interests include applications of power electronics in modern energy conversion systems and microgrids.

Dr. Mirafzal was a recipient of the 2008 second best IEEE Industry Applications Society Transactions Prize Paper Award published in 2007, the best 2012 IEEE Power and Energy Society Transactions Prize Paper Award published in 2011, and a 2014 U.S. National Science Foundation CAREER Award. He has served as the Technical Co-Chair of the IEEE IEMDC Conference in 2009 and currently serves as an Associate Editor for the IEEE TRANSACTIONS ON INDUSTRY APPLICATIONS and IEEE TRANSACTIONS ON POWER ELECTRONICS.